

# Human-Assisted Robotic Detection of Foreign Object Debris Inside Confined Spaces of Marine Vessels Using Probabilistic Mapping

Benjamin Wong<sup>a</sup>, Wade Marquette<sup>a</sup>, Nikolay Bykov<sup>a</sup>, Tyler M. Paine<sup>b</sup>,  
Ashis G. Banerjee<sup>a,c,\*</sup>

<sup>a</sup>*Department of Mechanical Engineering, University of Washington, Seattle, WA 98195, USA*

<sup>b</sup>*Naval Undersea Warfare Center Division Keyport, Keyport, WA 98345, USA*

<sup>c</sup>*Department of Industrial & Systems Engineering, University of Washington, Seattle, WA 98195, USA*

---

## Abstract

Many complex vehicular systems, such as large marine vessels, contain confined spaces like water tanks, which are critical for the safe functioning of the vehicles. It is particularly hazardous for humans to inspect such spaces due to limited accessibility, poor visibility, and unstructured configuration. While robots provide a viable alternative, they encounter the same set of challenges in realizing robust autonomy. In this work, we specifically address the problem of detecting foreign object debris (FODs) left inside the confined spaces using a visual mapping-based system that relies on Mahalanobis distance-driven comparisons between the nominal and online maps for local outlier identification. Simulation trials show extremely high recall but low precision for the outlier identification method. The assistance of remote humans is, therefore, taken to deal with the precision problem by going over the close-up robot camera images of the outlier regions. An online survey is conducted to show the usefulness of this assistance process. Physical experiments are also reported on a GPU-enabled mobile robot platform inside a scaled-down, prototype tank to demonstrate the feasibility of the FOD detection system.

*Keywords:* Robotics in hazardous fields, Mapping, Human-in-the-loop decision making

---

\*Corresponding author; Email address: ashishb@uw.edu

---

## 1. Introduction

Most large marine vessels are complex systems that operate in extreme open-ocean environments. As a result, they require significant cost and effort to maintain (inspect and repair), especially as the vessels age. For example, the total maintenance cost of the US Navy vessels was approximately 20 billion US dollars in 2020 [1], and this cost is projected to increase as the size of the fleet increases. Some of the most challenging maintenance tasks occur inside large tanks and other confined spaces inside the vessels. In particular, the vessels contain numerous “grey-water” tanks that can be fully or partially filled with seawater when the vessels are underway. The tanks provide critical access to much of the machinery on the vessels, but are difficult and dangerous spaces for humans to access. Often, these tanks are filled with pipes, cables, beams and other structural elements that are critical to the operation of the vessel, but are usually not arranged in an optimal way to allow a human to easily move and navigate through the confined space. Given these hazards, there is a lot of potential to use robots to perform many of these tasks.

However, there are two major challenges in achieving a viable robotic solution for this problem. First, the interiors of these confined spaces are often discolored, poorly illuminated and unstructured, which cause issues for traditional vision-based localization, mapping and navigation approaches. Second, the spaces are often irregularly shaped and cluttered with structural elements, as mentioned before. Therefore, it is difficult even for a robot to move inside the tank and access all the components, rendering robust locomotion and precise manipulation completely non-trivial.

A number of potential solutions have been explored to address the locomotion challenge, albeit for other types of confined spaces. For example, a quadruped climbing robot with a compliant magnetic foot has been developed to squeeze through entry portholes [2]. Different robot designs have been investigated for in-pipe inspection, including a composition of active and passive compliant joints [3], snake locomotion patterns [4] and adhesion-based crawling motions [5]. Various solutions have also been proposed to deal with the manipulation challenge. Representative examples include human-robot mixed-initiative control trading [6] and task dynamics imitation learning [7] for manufacturing inside confined spaces and a full stack autonomy

framework for multi-task manipulation of irregular objects [8].

We, instead, focus on the first challenge of robot localization, mapping and navigation inside confined spaces, and aim to decouple these capabilities from that of locomotion and manipulation. In other words, our methods are designed to be used on any robot with on-board processing and payload carrying capacity, including those with novel locomotion and manipulation capabilities. In this connection, there are several related works, including semi-automated inspection of an industrial combustion chamber [9]; submerged building mapping by an autonomous vehicle [10]; UAV-based localization in ballast tanks [11]; intelligent exploration in mines using a small drone [12]; autonomous navigation through manhole-sized confined spaces using a collision-tolerant aerial robot [13]; and, semi-autonomous inspection of underground tunnels and caves [14].

We, however, address the specific task of detecting foreign object debris (FOD) left inside large water tanks. While the FOD detection problem has been studied widely in the literature, almost all the studies are for open spaces, especially airports, where the presence of such debris is particularly detrimental. Recent examples of airport FOD detection methods include deep learning for standard optical cameras [15, 16, 17]; fractional Fourier transform [18], power spectrum features-based classification [19], cross section characteristics [20], line of sight visibility analysis [21], adaptive leakage cancellation [22], and variational mode decomposition [23] for frequency modulated continuous mm-wave radars; object minimal boundary extraction for infra-red cameras [24]; and, scan or point cloud processing for light detection and ranging (LiDAR) sensors [25, 26].

Other open space FOD detection applications include inspection of aircraft damages [27] and power transmission lines [28, 29], and real-time logistics monitoring [30] with visible light cameras. For confined space FOD detection, to the best of our knowledge, there has been only one reported work so far, where Latimer investigated processing of depth camera images for aircraft wing inspection [31]. On a somewhat related note, real-time detection of the differences of industrial parts from their corresponding computer-aided design (CAD) models has been done by processing the point clouds generated by hand-held laser scanners [32].

Here, we present a new confined space FOD detection system using point cloud-based representations of the visual maps generated by an autonomous ground robot. The online maps are compared with the existing CAD models or offline maps of FOD-less spaces, using a robust Mahalanobis distance-

based local outlier detection method. Simulation trials show very high recall rates but limited precision. We then conduct a human subjects experiment to show how the precision issue is addressed by taking the assistance of remote humans, who are able to reliably detect whether FODs are present, and, if so, what their types are, by looking at the close-up camera images of the outlier regions. We also perform experiments on a physical robot inside a prototype confined space to demonstrate the viability of the system. We, therefore, believe that our system would be useful for a wide range of challenging confined space inspection tasks, not just in marine vessels, but in other large vehicles, such as aircraft, military tanks and spaceships, with similar hazardous conditions.

## **2. Preliminaries**

A CAD model of a generic water tank was developed by the Naval Undersea Warfare Center (NUWC) Division Keyport to generate a realistic environment of a typical confined space found inside large vessels. The generic water tank model, as shown in Fig. 1, included many beams, piping, cabling, and other structures commonly used in ship construction. Although this CAD model was intended to be an accurate representation of the challenging environment encountered during maintenance activities in confined spaces, it was not a precise replication of any existing vessel space. Therefore, this CAD model was publicly released and is widely available for use by other researchers.

Technically, a FOD is any object that is alien to the environment, in this case the water tank. FOD has the potential to cause damages to the system during operation and must be removed via inspection. In a marine vessel, most common FODs include various standard hand tools, such as screwdriver and wrench, which are left behind after maintenance and repairs. In this paper, a FOD is simplified to include anything deviating from the given CAD model, which would primarily be a traditional FOD but could also include installation mismatch, tank defect or tank damage.

## **3. Technical Approach**

To accomplish effective and efficient inspection, we incorporate human-in-the-loop decision making to assist the semi-autonomous inspection system. The system is primarily running online under the Robot Operating System

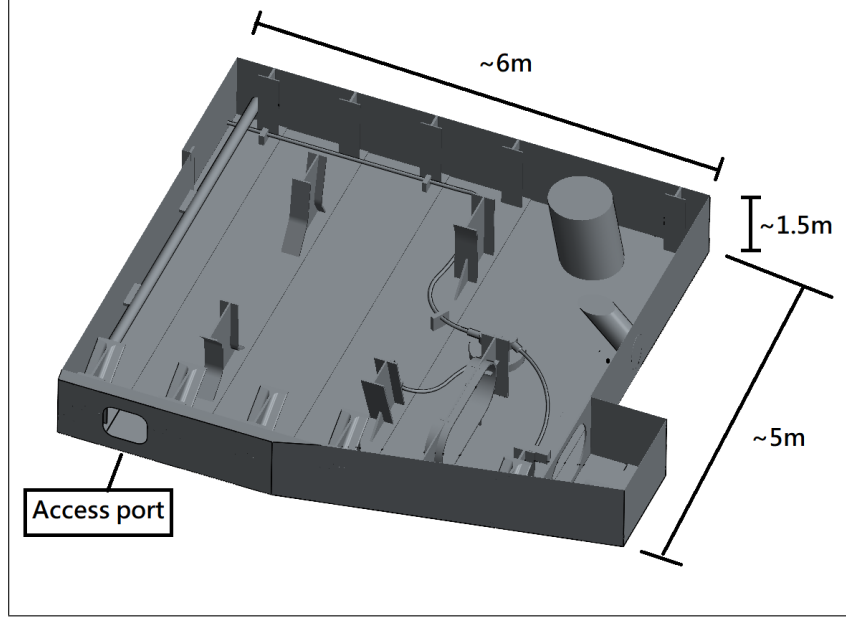


Figure 1: CAD model of a generic water tank with the roof not shown to allow viewing of the interior components

(ROS) framework, with various offline pre-processing modules to enhance the online performance. Pre-processing includes generating a look-up table for FOD candidate identification; and, defining an inspection route for every inspection session. The online inspection is sectioned into five major phases, as illustrated in Fig. 2. These phases consist of initial teloperation while the tank is being mapped out; three stages of autonomy comprising SLAM, FOD candidate identification, capturing of candidate FOD photos; and, human determination of FOD presence and type given point clouds of mapped tanks with highlighted candidate FODs and their corresponding photos. The technical details of the major processing modules and inspection phases are described next.

### 3.1. SLAM and Navigation

The SLAM functionality is provided by RTAB-Map via ROS [33]. The main objectives for the SLAM are self-localization in the confined space, and construction of point cloud for each inspection session using a 3D camera. RTAB-Map is chosen based on its open source ROS implementation, a wide variety of sensor compatibility, and good reported performance on many

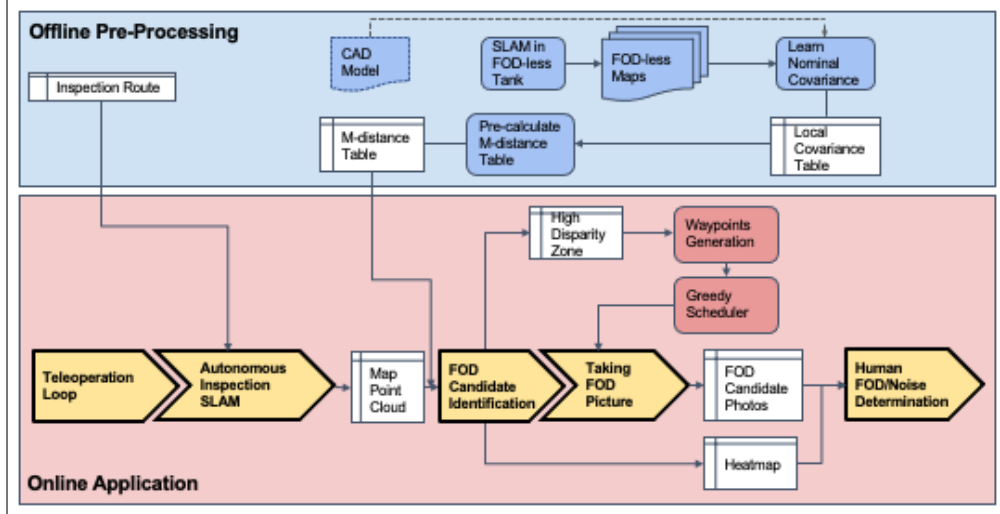


Figure 2: Overall pipeline of the FOD detection system

different tasks. In addition, RTAB-Map has a modular approach toward odometry and SLAM, which allows a simple switch between wheel odometry, in-built visual odometry, or any other third party odometry algorithm without affecting the SLAM functionality.

The navigation functionality is provided by the ROS navigation stack in the TurtleBot3 package. The navigation stack takes the 2D occupancy grid map generated by the SLAM package as an input and creates a 2D occupancy grid cost-map in real-time. Once a waypoint is published to the waypoint topic, the optimal trajectory from the current location to the specified waypoint is calculated and executed through velocity control.

### 3.2. FOD Candidate Identification

We develop our own FOD candidate identification algorithm to detect potential foreign objects from the point cloud generated by the SLAM module while preventing misclassification due to noise. The fundamental concept is to compare the discrepancy of each point in the point cloud to a known nominal map of the environment. The nominal map is either created using the mesh of the CAD model or through post processing of the collected sample point clouds. The nominal map is treated as the ground truth and any points that deviate from the nominal map by more than the cutoff value are considered FOD candidate points. The correspondences from the point cloud to the nominal map are drawn based on the nearest neighbors after the

initial point cloud registration. The deviation of each point is then calculated with respect to its corresponding point.

The CAD mesh option assumes that a accurate model of the environment is available, wherein, the CAD model is first exported as a PLY format triangle mesh and the mesh is uniformly sampled to create a dense point cloud. The sample point clouds option is developed for use in a confined space that contains a large number of unmodeled structures and/or manufacturing defects with respect to its CAD model. In this case, all the sample point clouds from the inspection training sessions are registered, either with the CAD model or one of the sample clouds. Next, all the sample clouds are merged into a single point cloud. The merged point cloud is then voxel down-sampled to calculate the mean points occupying a single voxel. This down-sampling process merges all the points in a voxel into a single point regardless of the number of points. However, this results in noisy points creating false voxel occupancy conditions. To eliminate this effect, a nearest neighbor search from the merged point cloud to the down-sampled point cloud is performed, and all the voxel points with nearest neighbor counts less than the 50th percentile are removed.

The deviation metric is a scalar value assigned to each point in a point cloud. The metric scales according to the estimated amount of deviation of these points to their corresponding points in the nominal point cloud. Euclidean distance for nearest neighbors is used as the *de facto* metric while comparing two point clouds. In our case, we consider the nearest neighbors of the points in the query point cloud to the nominal point cloud. However, this consideration often leads to noisy mapping of the walls and beams with high deviation values and either a) cause a large number of FOD candidates for a low distance threshold; or, b) are insensitive to small sized FODs for a high distance threshold.

We address this issue by using a probabilistic approach based on local *Mahalanobis distance* (M-distance). Alternatively, a spatial Chi-squared test can be used for local outlier detection [34]; however, it works well only for homogeneous density point clouds.

$$D_M = \sqrt{(x - \mu)^T \Sigma^{-1} (x - \mu)}. \quad (1)$$

The M-distance  $D_M$ , shown in (1), introduces an expected noise in the form of the covariance matrix  $\Sigma$ . It also adds directionality to the expected noise, which is especially useful in distinguishing the walls (with horizontal deviations) and beams (with vertical deviations). While  $\mu$  is defined as the closest

point from the training or query cloud point  $x$  to the nominal point cloud,  $\Sigma$  has to be estimated from the training samples. Therefore, a set of training maps are made by executing SLAM in an empty (FOD-less) tank with the same routes as those during inspection.

Instead of estimating one single global covariance matrix for the whole tank, we, instead, compute local covariances. It is done by first calculating the signed spatial error

$$\Delta x_{i,j} = \begin{pmatrix} x_j \\ y_j \\ z_j \end{pmatrix} - \begin{pmatrix} x_i \\ y_i \\ z_i \end{pmatrix} \quad (2)$$

from each point  $x_j$  on the sample point clouds to their nearest neighbor point  $x_i$  on the nominal point cloud. Next, for each point on the nominal point cloud that contains at least one sample point, we calculate the scatter matrix as:

$$n_i \Sigma_i = \sum_j (\Delta x_{i,j}) \cdot (\Delta x_{i,j})^T. \quad (3)$$

If this quantity is divided by the number of samples  $n_i$ , we get the maximum likelihood estimation (MLE) of the covariance for that point on the nominal map  $\Sigma_i$ . It is, however, deliberately left undivided to smooth out the covariance matrices within a local region. Otherwise, depending on the number of training maps, the point density of each training map and the voxel size of the nominal map, we risk having a large number of points on the nominal map with zero sample size and many points with a low sample size.

We consider two options for smoothing: mean smoothing and Gaussian smoothing. For mean smoothing, the covariances,  $\Sigma_{i,m}$ , are calculated regardless of the distance of the neighboring points to the center point using the formula:

$$\Sigma_{i,m} = \frac{1}{\sum_{j=1}^k n_j} \sum_{j=1}^k n_j \Sigma_j. \quad (4)$$

Here,  $k$  is the number of neighbors around the  $i$ -th point on the nominal map,  $n_j$  is the numbers of samples of the neighbors, and  $\Sigma_j$  is the covariance of the  $j$ -th neighbor. For Gaussian smoothing, the covariances,  $\Sigma_{i,G}$ , are computed similarly but with the distances of the neighbors modeled as reliability weights [35]. This weighting is based on a Gaussian kernel and a



tunable roll-off rate parameter  $\sigma$  as:

$$w_j = \exp \left[ -\frac{\|\Delta x_{i,j}\|^2}{\sigma^2} \right] \quad (5)$$

$$V_1 = \sum_{j=1}^k n_j w_j \quad V_2 = \sum_{j=1}^k n_j w_j^2 \quad (6)$$

$$\Sigma_{i,G} = \frac{1}{V_1 - V_2/V_1} \sum_{j=1}^k w_j (n_j \Sigma_j). \quad (7)$$

To define the smoothing neighborhood, we consider two alternatives:  $k$ -nearest neighbor and spherical region of interest.

Prior to smoothing, an optional voxel down-sampling step is performed on the nominal point cloud. In that case, a nearest neighbor search is performed to find the closest point from the full point set to the down-sampled point set. The covariances for the points in the full point set are then simply equal to the covariances of their nearest neighbors. Fig. 3 shows an example heat map of the Frobenius norm of the local covariances in the tank using down-sampling and Gaussian smoothing. The beam regions have a higher noise level and the ground is relatively less noisy as expected.

To avoid repeated matrix multiplications and nearest neighbour searches on a dense point cloud, a lookup table is calculated offline for the deviation metric. A three-dimensional mesh grid is created according to the dimensions of the water tank. The mesh grid is treated as a point cloud, and the deviation metric for each point is calculated and saved as a 3D table. For online mapping, the deviation metric for any point cloud is simply calculated by trilinear interpolation from the lookup table. To further reduce high deviation from sparse noise, a scalar version of the smoothing scheme similar to the covariance smoothing is applied on the deviation metric for each point in the cloud. This effectively removes the low density points from the list of FOD candidates.

Every point in the cloud with a deviation higher than the threshold is segmented out from the point cloud and clustered into FOD candidates using hierarchical clustering. The centroid of each cluster is then sent to the waypoint generation algorithm to proceed to the photo taking phase. Figure 4 shows an example of segmented and clustered FOD candidates point cloud, with the points lower than the threshold colored dark grey and each FOD candidate cluster colored in a different hue.

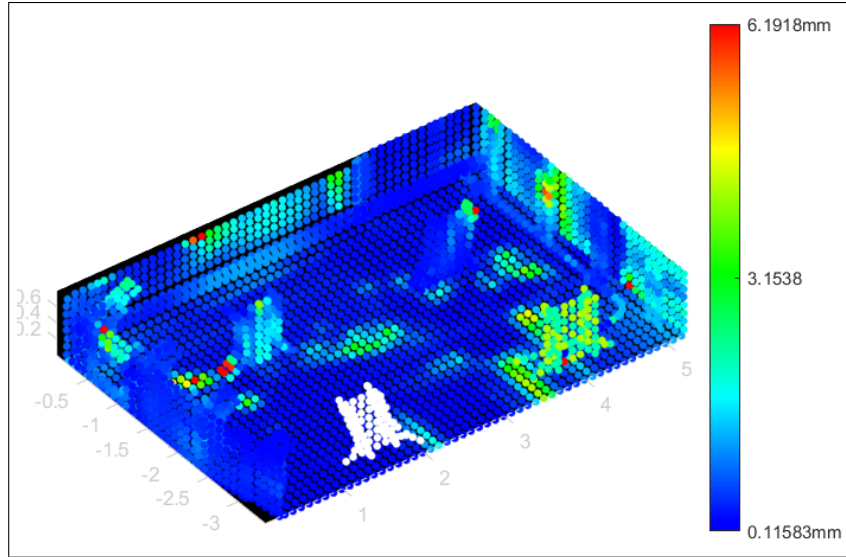


Figure 3: Heatmap of the Frobenius norm of the local covariance matrix in an empty (FOD-less) water tank with white indicating undefined value

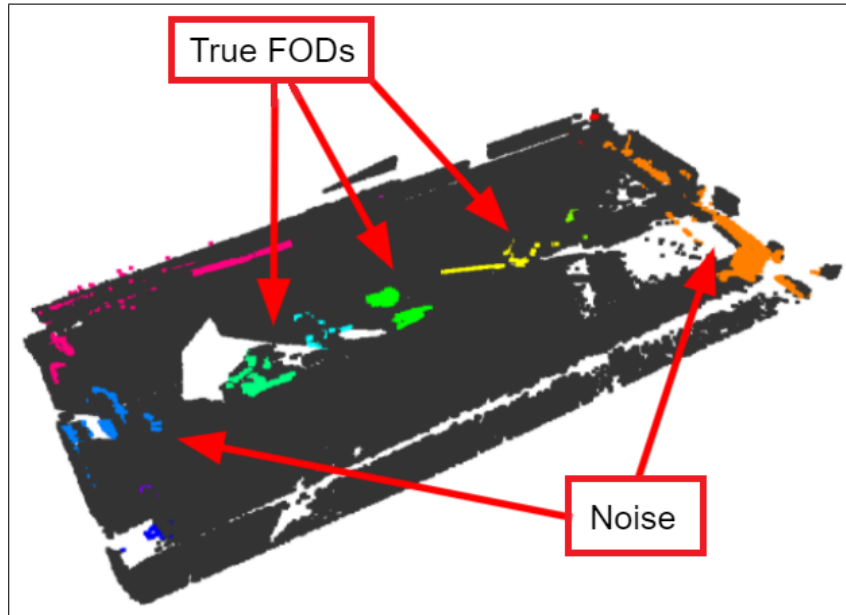


Figure 4: Point cloud with the high M-distance points clustered into different candidate FOD regions with each cluster shown using a distinct hue

### 3.3. Waypoint Generation

Once the FOD candidate locations are computed, they are passed to the waypoint generation module. First, candidate waypoints are created surrounding the FOD location within a minimum and maximum range so as to provide an acceptable image of the FOD. The candidate waypoints are then filtered to avoid colliding with the surroundings and ensure that the FOD is visible. To avoid collisions, the waypoints that overlap with high-cost regions of the cost-map are removed. To ensure that the FOD is visible, each remaining waypoint casts a ray between itself and the FOD. Here, a predefined cost-map from the FOD-less CAD model is used so that the rays are not penalized for viewing the FOD. The ray is terminated if it collides with surroundings in the FOD-less cost-map, and the corresponding waypoint is removed. Each ray records its cumulative cost, which is the sum of the cost in the grid cell under the ray at each time step. The candidate waypoint with the least cost is chosen as the final waypoint. The final waypoint will be the closer waypoint unless its view is more obstructed than a further waypoint. Figure 5 shows an example of the waypoint generation process; the orange band of waypoint candidates is first sampled around the FOD, many of the candidates are eliminated based on the cost map, and the waypoint with the least ray-casting cost is selected.

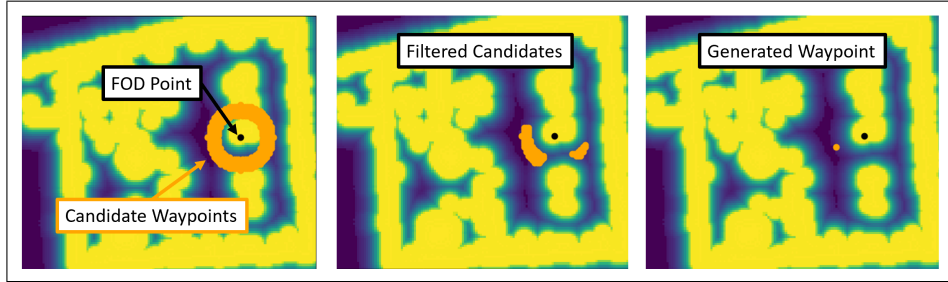


Figure 5: Autonomous waypoint generation given FOD location

## 4. Experiments

The experiments consist of two components: simulation trials with a human subjects study and physical trials on a scaled-down tank prototype.

#### 4.1. Simulation

The simulation was done using Gazebo in Ubuntu with ROS Melodic as the framework and Python as the programming language. The CAD model of the tank was painted with a rusty white texture and exported as a DAE file using Blender. The DAE file was spawned in Gazebo with all the natural light sources disabled to recreate the dark confined space environment. TurtleBot3 Waffle Pi was chosen as the robot model and was modified with the monster wheel from the TurtleBot3 Friends section. The original Pi camera was replaced by two identical cameras using Intel RealSense D435’s stereo camera specifications. A spot light source was added to the front of the robot to act as a flashlight.

The experiments comprised a total of 30 trials, with 15 trials using the RTAB-Map’s built-in visual odometry and another 15 trials using the robot’s wheel odometry. For each trial, the robot was spawned near the access hole with the same pose. In addition, two to five FODs were randomly spawned with random poses from a pool of six FOD types, consisting of drill, screw driver, hammer, wrench, level, and sander. Point cloud registration was performed using the Open3D iterative closest point (ICP) method. For candidate FOD identification, we enabled down-sampling with a ratio of 0.1, and used the M-distance to CAD model option with Gaussian smoothing ( $\sigma = 0.05$ ), a spherical region of interest (radius of  $4\sigma$ ), and a cutoff distance of 1.75.

The resultant FOD photos were assembled into online questionnaire surveys, with each survey containing all the photos from a single trial. The administration of the anonymous survey was approved by the University of Washington (UW) Institutional Review Board with the study # STUDY00013902. The surveys were sent out to UW students and Naval Undersea Warfare Center (NUWC) Division Keyport personnel. A total of 23 responses were received, of which 61.9% were engineers, 33.3% graduate students, and 4.8% managers. 57.1% were in the 18-30 age group, 28.6% in the 31-45 group, and 14.3% in the 46-60 group. 81.0% of the participants were males and 19.0% were females.

We first analyzed the performance of the FOD detection approach before looking at the effectiveness of remote humans in making the final decisions. Table 1 shows the total number of FODs generated for the trials and the photos taken by the robot during the trials for the two odometry methods. Visual odometry has a slightly higher photo per FOD ratio than that of wheel odometry. This is expected due to higher localization uncertainty in

visual odometry, which increases the number of high deviation point clusters associated with the robot pose.

Table 1: No. of FOD candidate photos taken during simulation trials

	<b>Total FOD</b>	<b>Photos Taken</b>	<b>Photos/FOD</b>
<b>Wheel Odometry</b>	54	168	3.11
<b>Visual Odometry</b>	52	186	3.51

The relevance of the FOD photos is shown in Table 2, where the “photo contains FOD” category includes the same FOD appearing in multiple photos and photos containing partial FOD images. The precision of the odometry method is defined as the number of photos containing FODs divided by the total number of photos. It is less than 50% for both the odometry methods, with wheel odometry being slightly lower than visual odometry. This low value is a direct result of high sensitivity by choosing a low M-distance threshold. This trade-off is deliberate considering that humans are involved in final decision making and low precision would increase their workload, whereas, a failure to capture potential FODs would lead to missed detections. Figure 6 shows an example of a photo containing FOD, with a gray screwdriver at the center of the image, and an example of a photo with no FOD, which is a false positive detection due to the noise associated with the I-beam structure.

Table 2: Relevance of candidate FOD photos

	<b>Contains FOD</b>	<b>No FOD</b>	<b>Photo Precision</b>
<b>Wheel Odometry</b>	64	104	0.381
<b>Visual Odometry</b>	77	109	0.414

The effect of high sensitivity, or recall, is shown in Table 3. The first column shows the total number of FODs detected by the photo set, which is the number of FODs present in a session and captured in at least one photo. This differs from the photo containing FOD in that only distinct FODs are counted here. The second column shows the number of missing FODs, which are FODs present in a session but not seen in any of the photos. The detection rates are high as previously discussed, with both the odometry methods having recall greater than 90%. This suggests that if the human



Figure 6: Examples of candidate FOD photos, taken by the inspection robot, that are shown to remote humans for final decision-making.

are able to spot all the FODs in the photos, over 90% of the FODs can be detected and removed afterward.

Table 3: FOD Detection Rate

	Detected FOD	Missed FOD	FOD Recall
<b>Wheel Odometry</b>	51	3	0.944
<b>Visual Odometry</b>	48	4	0.923

Table 4 shows the confusion matrix of the study participants in labeling each photo as “having FOD” or “not having FOD” with “having FOD” being positive. The accuracy is high for both the positive and negative labels as seen in the diagonal entrees. The overall accuracy of detecting the presence of a FOD is 0.948, whereas, the accuracy of identifying the exact FOD type comes out to be 0.860. The confusion matrix for exact FOD labeling is reported in Table 5. Unlike standard confusion matrices, the labels contain a “not sure” option for participants that find a FOD but cannot identify it. We also have a “mixed FOD” column to include photos with multiple detected FODs and multiple mislabeled FODs, since it is not possible to deduce which FOD is causing the confusion. As before, the matrix shows a high labeling accuracy with the maximum values in the diagonal entries.

As reported in Table 5, the spirit level is the most confused FOD, which is likely due to a low-quality rendering of the level. Figure 7 shows an example of such a confusing photo, with the level colored uniformly red. While the color red is easy to spot in the photos, the detailed shape is hard to see with

Table 4: Confusion Matrix of Human Labeling

	Actual Positive	Actual Negative
Labeled Positive	112	4
Labeled Negative	11	160

Table 5: Confusion Matrix of Human Labeled FOD types

		Actual Type							
		Hammer	Level	Screwdriver	Wrench	Sander	Drill	No FOD	Mixed FOD
Labeled Type	Hammer	6	0	0	0	0	0	0	1
	Level	0	17	0	0	0	0	0	0
	Screwdriver	0	0	33	0	0	0	0	0
	Wrench	0	0	0	20	0	0	0	0
	Sander	0	0	0	0	2	0	0	0
	Drill	0	0	0	0	0	11	0	0
	No FOD	0	0	1	4	6	0	163	0
	Not Sure	2	13	0	8	1	2	3	0

uniform coloring, which makes the level appear as a red bar from a distance. On the other hand, the item most comomly mislabeled as “No fod” is the sander. Similar to the spirit level, the sander has a less distinct outline as compared to the other FODs. However, unlike the bright red color of the level, the sander is colored dark gray, as shown in Fig. 7, which makes it similar to the hue of the rusty tank texture. Hence, it is quite easy for the participants to completely miss the sander.

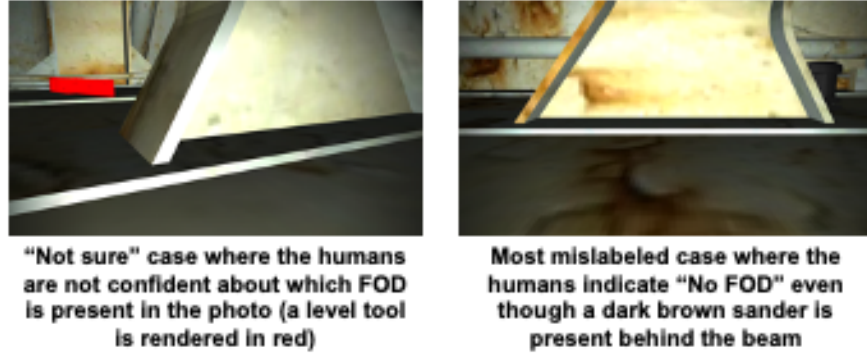


Figure 7: Candidate FOD photos causing maximum confusion to the human subjects during online questionnaire survey

We also compared the various candidate FOD identification methods with no voxel down-sampling. The segmentation threshold values were based on

the first trial cloud such that all the FODs were completely segmented from the rest of the tank. Table 6 shows the comparison results. While the CAD nearest neighbor (NN) and the CAD M-distance methods yield a similar number of FOD candidates, they show a significant difference in the total number of segmented points. The CAD NN method generates a much larger number of false positive points, which not only reduces precision but also poses problems to the clustering method, as discussed later in Section 5. The point cloud M-distance method performs much better than the other two methods with respect to both the number of FOD candidates and the number of segmented points.

Table 6: Comparisons of Different FOD Candidate Detection Methods

	<b>CAD NN</b>	<b>CAD M-Distance</b>	<b>Point Cloud M-Distance</b>
<b>Total No. of Candidates</b>	167	164	91
<b>No. of Points Per Trial</b>	86,145 $\pm 61,124$	56,780 $\pm 49,677$	18,553 $\pm 15,676$

#### 4.2. Physical Trials

A modified TurtleBot 3 Waffle Pi was used as the robot platform. Instead of using the baseline Raspberry Pi 3B+, an Nvidia Jetson AGX Xavier was added to the robot to provide on-board GPU capability. The default Pi camera was also replaced by a RealSense D435i depth camera. As shown in Fig. 8, a scaled down prototype of the water tank was built from ply wood and painted with a white base with rusty brown spots to mimic the actual tank texture. The tank pillars were removed due to the current limited mobility of the robot platform caused by the power supply, HDMI, and Ethernet connection cables. We also tested the FOD detection capability using simple teleoperation routes without autonomous navigation due to this mobility issue.

First, a training set was created by driving the robot ten times along each of the two routes shown in Fig. 8. Three FOD scenarios were considered as a part of testing: 1) a power drill placed at the end of route 1; 2) a power drill kept at the end of route 2; and, 3) a sander placed at the end of route 1. Three test trials were done for each scenario and Fig. 9 shows representative results for the different candidate FOD detection methods.



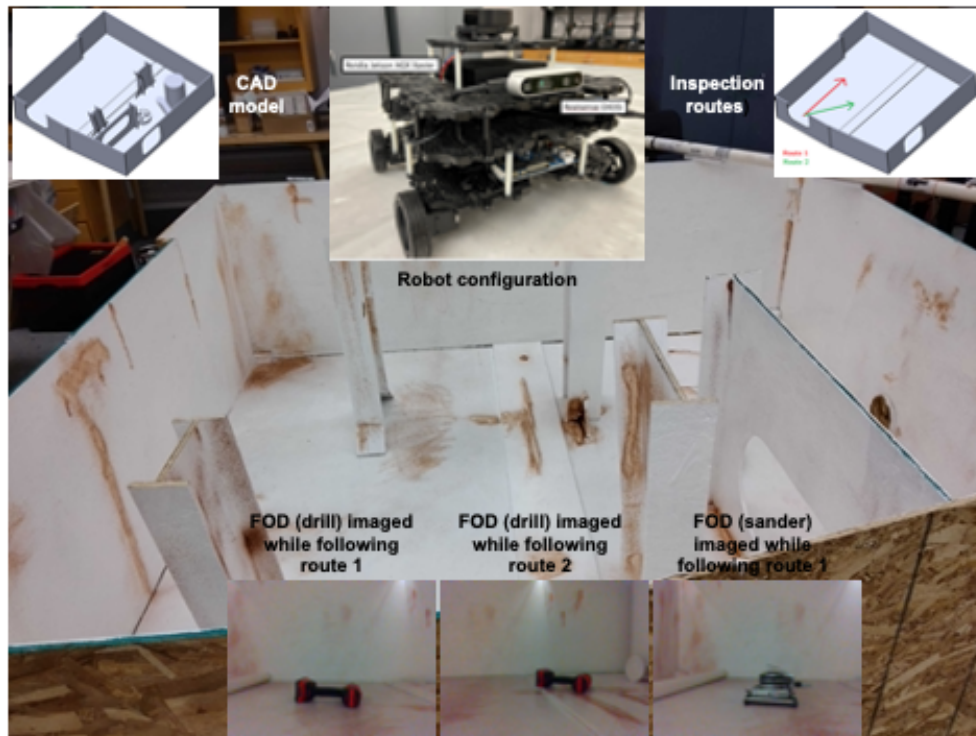


Figure 8: Simplified and scaled-down water tank model (without the top cover but including the pillars), robot platform and inspection routes for physical trials

Unlike simulation, here, mean smoothing was applied along with  $k$ -nearest neighbor ( $k = 250$ ). The FODs are visualized using hue heatmaps, with blue and red indicating low and high distances, respectively. The mapping from the distance metric to the hue is normalized such that the FOD in the first training run is completely red. Overall, as hypothesized, we observe that the local M-distance methods provide greater robustness to detection noise than the CAD NN method since the learned covariance matrices are able to accommodate the consistent noise terms during training. Moreover, the point cloud M-distance method performs better than its CAD counterpart as the CAD model is quite inaccurate relative to the built prototype. Route 2 is a particularly challenging example due to the visibility of large unmodeled structures, especially a column on the right hand side of the map. In this case, the M-distance methods also encounter difficulties as the noise patterns are different in each trial due to slight variations in the executed robot routes. All the methods perform quite well for the sander example, indicating that, as expected, FOD detection is facilitated by relatively accurate point clouds.

## 5. Discussion

There are a few limitation of our approach, as seen in the experimental results. The primary assumption of using M-distance is that the deviation from the nominal model is Gaussian. However, there are multiple sources of non-Gaussian noise during the SLAM process. One source is localization uncertainty, which causes feature duplication at the erroneous robot location. This poses problem when using the M-distance as it treats the entire duplicate feature as deviation and causes false positives. Another problematic noise type is associated with the depth camera, which occurs around the edge of an object where the depth gradient is very high. Normally, the edge noises are removed during the SLAM process when the robot travels behind the obstacles. However, this does not happen for confined space structures such as the I-beam on the wall. These noise sources can be potentially dealt with by transitioning to non-Gaussian learning methods such as mixture models.

The clustering method also introduces an error in conjunction with this duplicated feature problem. When there is a large patch of false positive points, the hierarchical clustering algorithm sometimes clusters the true FOD points with the false positive points into one group. As a result, the center of the cluster mass for the waypoint generating algorithm meanders more toward the false positive, and sometimes causes the true positive to disap-

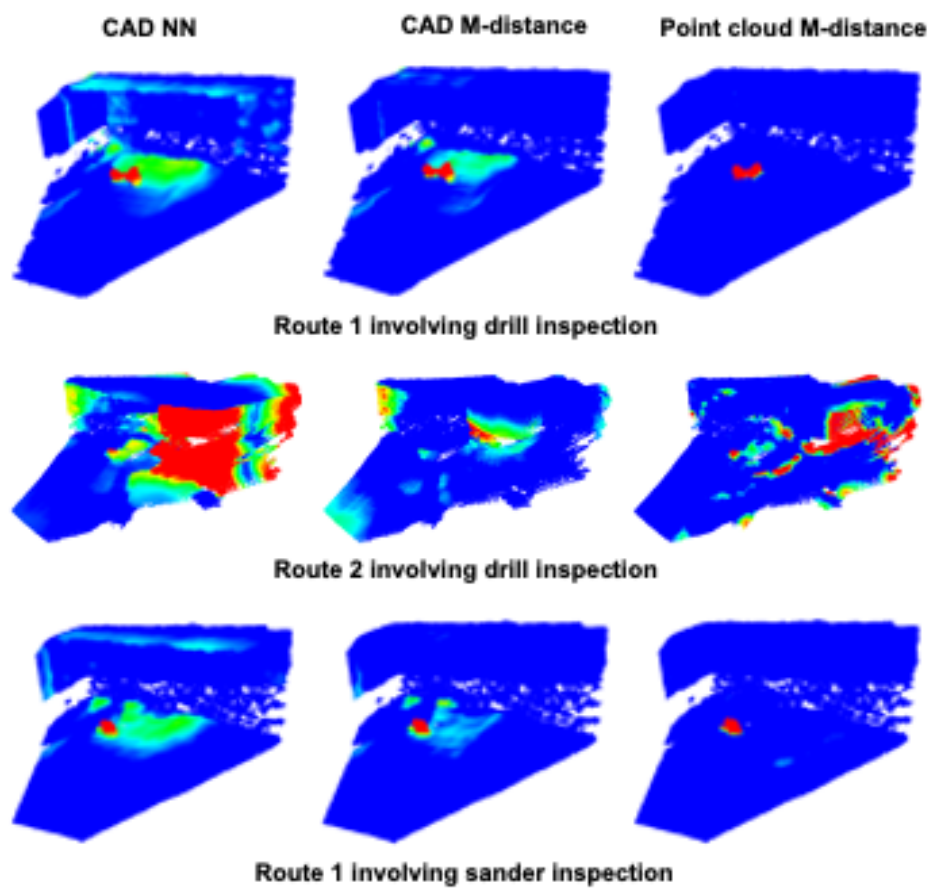


Figure 9: Examples of heatmaps indicating potential occurrences of two types of FODs by the physical robot using the different detection methods.

pear from the camera’s field of view. A work-around for this issue could be including the cluster size information during waypoint generation.

Smoothing is also found to have a major impact on the quality of the covariance map during the training session with the simpler mean smoothing providing better numerical stability. For Gaussian smoothing, problem occurs when a region has a low sampling rate and the nearest valid neighbor is several standard deviations away from the sample under consideration. Due to the rapid roll-off rate of the Gaussian function, the weight becomes very small, making the weighted mean numerically unstable. This can be mitigated by tuning the rate according to the density of the training point cloud to achieve an optimal balance between locality and numerical stability.

When parallel computing is not feasible, down-sampling is required to complete smoothing in a reasonable amount of time (tens of seconds). For example, in the simulation experiments, the point clouds are down-sampled to around 6,000-7,000 points and it takes around 30 seconds to process, and a raw cloud generally has points in the order of magnitude of  $10^5$ . Since smoothing is a convolution-like process, the time complexity scales roughly linearly with the number of query points. When parallel computing is available, down-sampling is still recommended but the number of allowable query points is substantially higher. In the current implementation,  $k$ -nearest neighbor search is still done serially for each query point, while the averaging process is parallelized.

## 6. Conclusions

In this paper, we propose a remote human-assisted, visual mapping-based probabilistic FOD detection system for confined spaces within large marine vessels. A generic water tank, with publicly released CAD model, is used as the representative confined space for system development and testing. A local Mahalanobis distance-driven outlier identification method forms the core of our system, which enables identification of candidate FODs by quantifying the discrepancies between the offline FOD-less maps (or, the tank CAD model) and the online maps acquired by an autonomous ground robot. While this method yields very high recall rates, precision is low, necessitating human assistance in labeling the candidate FOD images taken by the robot camera. We subsequently conduct an online study to highlight the effectiveness of the human assistance process. Physical experiments inside a scaled-down tank prototype further demonstrate the potential of our detec-

tion system. In the future, we would like to modify our system for other kinds of inspection tasks, such as identification and monitoring of tank defects and damages.

## Acknowledgment

We gratefully acknowledge John Stewart for his help in building the water tank prototype and Prof. Santosh Devasia for many useful discussions. Any opinions, findings, and conclusions or recommendations expressed in this paper are those of the authors and do not necessarily reflect the views of the US Navy.

## References

- [1] CBO, US Navy maintenance cost (2020).  
URL <https://www.cbo.gov/system/files/2019-10/55685-CBO-Navys-FY20-shipbuilding-plan.pdf>
- [2] T. Bandyopadhyay, R. Steindl, F. Talbot, N. Kottege, R. Dungavell, B. Wood, J. Barker, K. Hoehn, A. Elfes, Magneto: A versatile multi-limbed inspection robot, in: IEEE/RSJ Int. Conf. Intell. Robot. Syst., 2018, pp. 2253–2260.
- [3] A. Kakogawa, S. Ma, A multi-link in-pipe inspection robot composed of active and passive compliant joints, in: IEEE/RSJ Int. Conf. Intell. Robot. Syst., 2020, pp. 6472–6478.
- [4] I. Virgala, M. Kelemen, P. Božek, Z. Bobovský, M. Hagara, E. Prada, P. Oščádal, M. Varga, Investigation of snake robot locomotion possibilities in a pipe, *Symmetry* 12 (6) (2020).
- [5] E. Technologies, Versatrax pipe inspection crawler (2021).  
URL <https://eddyfi.com/en/application/pipelines>
- [6] P. Owan, J. Garbini, S. Devasia, Addressing agent disagreement in mixed-initiative traded control for confined-space manufacturing, in: IEEE Int. Conf. Adv. Intell. Mechatronics, 2017, pp. 227–234.
- [7] P. Owan, J. Garbini, S. Devasia, Faster confined space manufacturing teleoperation through dynamic autonomy with task dynamics imitation learning, *IEEE Robot. Autom. Lett.* 5 (2) (2020) 2357–2364.

- [8] Z. Han, J. Allspaw, G. LeMasurier, J. Parrillo, D. Giger, S. R. Ahmadzadeh, H. A. Yanco, Towards mobile multi-task manipulation in a confined and integrated environment with irregular objects, in: IEEE Int. Conf. Robot. Autom., 2020, pp. 11025–11031.
- [9] P. Tripicchio, M. Satler, M. Unetti, C. A. Avizzano, Confined spaces industrial inspection with micro aerial vehicles and laser range finder localization, *Int. J. Micro Air Veh.* 10 (2) (2018) 207–224.
- [10] V. Preston, T. Salumäe, M. Kruusmaa, Underwater confined space mapping by resource-constrained autonomous vehicle, *J. Field Robot.* 35 (7) (2018) 1122–1148.
- [11] R. Y. Brogaard, M. Zajaczkowski, L. Kovac, O. Ravn, E. Boukas, Towards UAV-based absolute hierarchical localization in confined spaces, in: IEEE Int. Symp. Safety Security Rescue Robot., 2020, pp. 182–188.
- [12] A. Akbari, P. S. Chhabra, U. Bhandari, S. Bernardini, Intelligent exploration and autonomous navigation in confined spaces, in: IEEE/RSJ Int. Conf. Intell. Robots Syst., 2020, pp. 2157–2164.
- [13] P. De Petris, H. Nguyen, T. Dang, F. Mascarich, K. Alexis, Collision-tolerant autonomous navigation through manhole-sized confined environments, in: IEEE Int. Sym. Safety Security Rescue Robot., 2020, pp. 84–89.
- [14] H. Azpúrua, A. Rezende, G. Potje, et al., Towards semi-autonomous robotic inspection and mapping in confined spaces with the EspeleoRobô, *J. Intell. Robot. Syst.* 101 (4) (2021) 69.
- [15] X. Cao, P. Wang, C. Meng, X. Bai, G. Gong, M. Liu, J. Qi, Region based CNN for foreign object debris detection on airfield pavement, *Sensors* 18 (3) (2018) 737.
- [16] Q. Gao, R. Hong, Y. Chen, J. Lei, Research on foreign object debris detection in airport runway based on semantic segmentation, in: 2nd Int. Conf. Comput. Data Sci., 2021, pp. 1–3.
- [17] Q. Gao, R. Hong, Y. Chen, J. Lei, Research on detection algorithm of foreign object debris and small targets in airport runway based on SSD, in: 2nd Int. Conf. Comput. Data Sci., 2021, pp. 1–4.

- [18] Y.-K. Lai, Foreign object debris detection method based on fractional Fourier transform for millimeter-wave radar, *J. Appl. Remote Sensing* 14 (1) (2020) 1 – 15.
- [19] P. Ni, C. Miao, H. Tang, M. Jiang, W. Wu, Small foreign object debris detection for millimeter-wave radar based on power spectrum features, *Sensors* 20 (8) (2020) 2316.
- [20] S. Futatsumori, N. Yonemoto, N. Shibagaki, Y. Sato, K. Kashima, Detection probability estimation of 96 GHz millimeter-wave airport foreign object debris detection radar using measured radar cross section characteristics, in: *Eur. Conf. Antennas Propag.*, 2021, pp. 1–4.
- [21] G. Fizza, S. M. Idrus, F. Iqbal, W. H. W. Hassan, N. Shibagaki, K. Kashima, A. Hamzah, S. Ambran, T. Kawanishi, Line of sight visibility analysis for foreign object debris detection system, *J. Phy.: Conf. Series* 1878 (1) (2021) 012006.
- [22] T. Liu, H. Cui, Y. Wang, M. Zhai, J. Zhang, Z. Wei, Adaptive leakage cancelation method in frequency modulated continuous wave radar for foreign object debris detection, *Int. J. RF Microw. C E* 31 (3) (2021) e22546.
- [23] J. Zhong, X. Gou, Q. Shu, X. Liu, Q. Zeng, A FOD detection approach on millimeter-wave radar sensors based on optimal VMD and SVDD, *Sensors* 21 (3) (2021) 997.
- [24] V. V. Kniaz, A Fast Recognition Algorithm for Detection of Foreign 3D Objects on a Runway, *ISPRS - Int. Archives Photogrammetry, Remote Sensing Spatial Inf. Sci.* XL3 (2014) 151–156.
- [25] J. Mund, A. Zouhar, L. Meyer, H. Fricke, C. Rother, Performance evaluation of LiDAR point clouds towards automated FOD detection on airport aprons, in: *Proc. Int. Conf. Appl. Theory Autom. Command Control Syst.*, 2015, pp. 85–94.
- [26] A. Elrayes, M. H. Ali, A. Zakaria, M. H. Ismail, Smart airport foreign object debris detection rover using LiDAR technology, *Internet Things* 5 (2019) 1–11.

- [27] H. Xu, Z. Han, S. Feng, H. Zhou, Y. Fang, Foreign object debris material recognition based on convolutional neural networks, *EURASIP J. Image Video Proc.* 21 (2018) 1–10.
- [28] W. Zhang, X. Liu, J. Yuan, L. Xu, H. Sun, J. Zhou, X. Liu, RCNN-based foreign object detection for securing power transmission lines (RCNN4SPTL), *Procedia Comput. Sci.* 147 (2019) 331–337.
- [29] S. Haotian, L. Tong, W. Pu, X. Liang, Z. Hongwei, Foreign object detection of electric transmission line with dynamic federated learning, *IOP Conf. Ser.: Earth Environ. Sci.* 791 (1) (2021) 012159.
- [30] H. Xiong, J. Wu, Q. Liu, Y. Cai, Research on abnormal object detection in specific region based on Mask R-CNN, *Int. J. Adv. Robot. Syst.* 17 (3) (2020) 1729881420925287.
- [31] K. Latimer, Remote visualization and detection of foreign object debris in aerospace manufacturing using a low-cost depth camera, Master’s thesis, University of Washington (2019).
- [32] S. Kahn, U. Bockholt, A. Kuijper, D. W. Fellner, Towards precise real-time 3D difference detection for industrial applications, *Comput. Ind.* 64 (9) (2013) 1115–1128.
- [33] M. Labbé, F. Michaud, RTAB-Map as an open-source lidar and visual simultaneous localization and mapping library for large-scale and long-term online operation, *J. Field Robot.* 36 (2) (2019) 416–446.
- [34] EDF, CloudCompare local statistical test (2020).  
URL [https://www.cloudcompare.org/doc/wiki/index.php?title=Local\\_Statistical\\_Test](https://www.cloudcompare.org/doc/wiki/index.php?title=Local_Statistical_Test)
- [35] M. Galassi, J. Davies, J. Theiler, B. Gough, G. Jungman, M. Booth, F. Rossi, Gnu scientific library- reference manual (2021).  
URL [https://www.gnu.org/software/gsl/doc/html/statistics.html#c.gsl\\_stats\\_wvariance](https://www.gnu.org/software/gsl/doc/html/statistics.html#c.gsl_stats_wvariance)